DYNAMICS OF LONGITUDINALLY FORCED BLUFF BODY FLAMES WITH VARYING DILATATION RATIOS

A Thesis
Presented to
The Academic Faculty

by

Dmitriy Vital Plaks

In Partial Fulfillment
of the Requirements for the Degree
Master of Science in the
School of Aerospace Engineering

Georgia Institute of Technology
December 2009

DYNAMICS OF LONGITUDINALLY FORCED BLUFF BODY FLAMES WITH VARYING DILATATION RATIOS

Approved by:

Dr. Timothy Lieuwen, Advisor
School of Aerospace Engineering
Georgia Institute of Technology

Dr. Jeff Jagoda
School of Aerospace Engineering
Georgia Institute of Technology

Dr. Suresh Menon
School of Aerospace Engineering
Georgia Institute of Technology

Date Approved: November 5, 2009

ACKNOWLEDGEMENTS

I would like to thank Dr Tim Lieuwen for providing research and academic guidance during my stay at Georgia Tech. I would also like to thank Christopher Brown, Ulises Mondragon and Dr Vincent McDonnell of Energy Research Consultants for providing the data used in this thesis. In addition, I would also like to thank Dr Santosh Shanbhogue, Bobby Noble, and other residents of the Georgia Tech Combustion Lab for their knowledgeable and always timely assistance as well as moral support. I would especially like to thank my parents, without whose guidance and support I would not be here.

TABLE OF CONTENTS

LIST OF TABLES

Page

LIST OF FIGURES

Page

NOMENCLATURE

Symbols

A	Area
D_{hub}	Swirler diameter
D_{sw}	Swirler hub diameter
d	Bluff body diameter
H	Burner height
h_R	Heat of reaction
I_t	Edge detection threshold
L	Flame position
$\dot{m}$	Mass flow rate
P	Pressure
Q	Flame luminosity
R	Gas constant
S_L	Flame speed
S_N	Swirl number
T	Temperature
t	Time
TF	Transfer function
u	Velocity in the x-direction
v	Velocity in the y-direction
W	Burner width
x	Direction along flow path
y	Direction perpendicular to flow path

θ	Flame angle
θ_m	Boundary layer momentum thickness
θ_s	Swirler blade angle
λ	Wavelength
ρ	Density
ϕ	Phase of flame wrinkle

Subscripts

b	Burned
c	Convective
d	(see above)
j	Fuel jet
m	Main flow
max	Maximum
P	Primary burner
Peak	Location of peak amplitude
S	Secondary burner
u	Unburned
v	velocity
θ_m	(see above)

Superscripts

’	Fluctuation
¯ (bar)	Mean

SUMMARY

This thesis focuses on experimentally measuring the response of varying dilatation ratio bluff body flames under harmonic excitation. Such flames are often encountered in jet engine afterburners and are susceptible to combustion instabilities. Previous work has been done modeling such flames, however, only limited experimental data has been obtained at these conditions and is the motivation for this thesis.

The focus of this work is to measure the transfer function of longitudinally forced, varying dilatation ratio bluff body flames. The transfer function is obtained by measuring flame position and flame luminosity fluctuations at the forcing frequency. Specifically, the amplitude and phase of the fluctuations are characterized as a function of flow velocity, axial location, and perturbation amplitude. These measurements are also compared to available theoretical predictions, showing that qualitative measured trends are consistent with theory. In addition, a detailed quantitative comparison is performed at one condition, showing good agreement between predictions and measurements in the near and mid-field of the flame response. However, agreement is not obtained in the far-field, indicating that continued theoretical work is needed to understand the flame response characteristics in this region.

CHAPTER 1

INTRODUCTION

Combustion instabilities have been an area of research interest for many decades. They are highly important in any kind of combustor as their presence affects combustor performance, shortens its life, and in some cases cause catastrophic failure. This is especially true in aircraft engine afterburners.

Understanding how the flame responds to disturbances is key to understanding combustion instabilities. Many studies have experimentally measured a flame transfer function for laminar flames [1-3], turbulent flames [4-7], premixed flames [2-6, 8-11], and diffusion flames [7, 12-14]. Many numerical and theoretical studies have also been done (see [15] for a good review on the subject). Lately, the focus has been on laminar premixed flames and their applicability in gas turbine combustors due to these flames being highly susceptible to instabilities. However, only limited data is available in the operating conditions of afterburners (see [16-18]). This lack of knowledge is the motivation for this study.

Before delving into experiments, it is important to understand the basic coupling mechanisms responsible for combustion instabilities. In the transfer function approach to studying the flame, the transfer function is defined as

$$TF = \frac{Q'/\bar{Q}}{u'/\bar{u}} \tag{1}$$

where Q is the heat release (transfer function output) and u is the velocity (transfer function input), prime quantities represent fluctuations and bar quantities represent time

averages. This approach assumes that both the velocity and heat release can be written using a Reynolds decomposition as

$$u(t) = u'(t) + \bar{u} \tag{2}$$

$$Q(t) = Q'(t) + \bar{Q} \tag{3}$$

While measuring heat release directly is not feasible, indirect techniques such as chemiluminescence or flame area measurements allow for a good approximation to the transfer function output.

Let us now look at the fluid mechanics of bluff body stabilized flames. In the limit case of $T_b/T_u = 1$ (i.e. no combustion), the flow field is divided in two separate regimes, shear layer and wake, each having their own characteristics [7, 12-14]. The shear layer is dominated by the Kelvin-Helmholtz (KH) instability characterized by symmetric vortex shedding from the bluff body [19]. The wake is dominated by the von-Kármán instability characterized by asymmetric vortices [20]. Increasing the temperature ratio, T_b/T_u, suppresses the von-Kármán mode; however, there is some disagreement as to what the critical temperature ratio is [21-23]. Since temperature ratio is a measure of heat release, it is clear that the addition of combustion drastically alters not only the flame dynamics but also the overall flow field.

The modeling of flame dynamics is done via the G equation, which predicts the position of the flame sheet. Although measuring flame luminosity is much easier, flame edge measurements are much more desirable as they allow direct comparison between theoretical predictions of the G equation.

The goal of this thesis is to measure the flame edge fluctuations and flame luminosity fluctuations of varying dilatation ratio bluff body flames under acoustic

forcing. Chapter 2 outlines the methodology used to measure the transfer function while Chapter 3 applies that methodology and shows flame edge fluctuations and luminosity fluctuations under longitudinal forcing at various flow conditions. The two methods are compared to each other and flame edge fluctuations are compared to theoretical predictions.

CHAPTER 2

EXPERIMENTAL METHODOLOGY

Experimental Facility

The following description closely follows prior publications of this facility [24], which is operated by Energy Research Consultants. Experiments are conducted in a premixed, atmospheric test rig (see Figure 1a) operated in both a vitiated and non-vitiated mode. The test section is 76.2 mm x 127 mm with a triangular bluff body of 32 mm wide and 51 mm high (Figure 1b). Air enters at the base of the setup and mixes with natural gas in the next chamber. After the mixture burns in the vitiator, dilution air is added and the flow passes through a pebble bed. Natural gas is added immediately after the pebble bed section. The flow passes through a converging section and a honeycomb flow straightener before entering the test section. The flow velocity at the bluff body lip varies from 18 m/s to 170 m/s and the inlet temperature into the test section varies from 310 K (non-vitiated) to 870 K (see Table 1).

Fuel concentration profiles are measured just upstream of the bluff body and spatial non-uniformities are less than 2% at 15 m/s and 20% at 190 m/s (the latter case is vitiated).

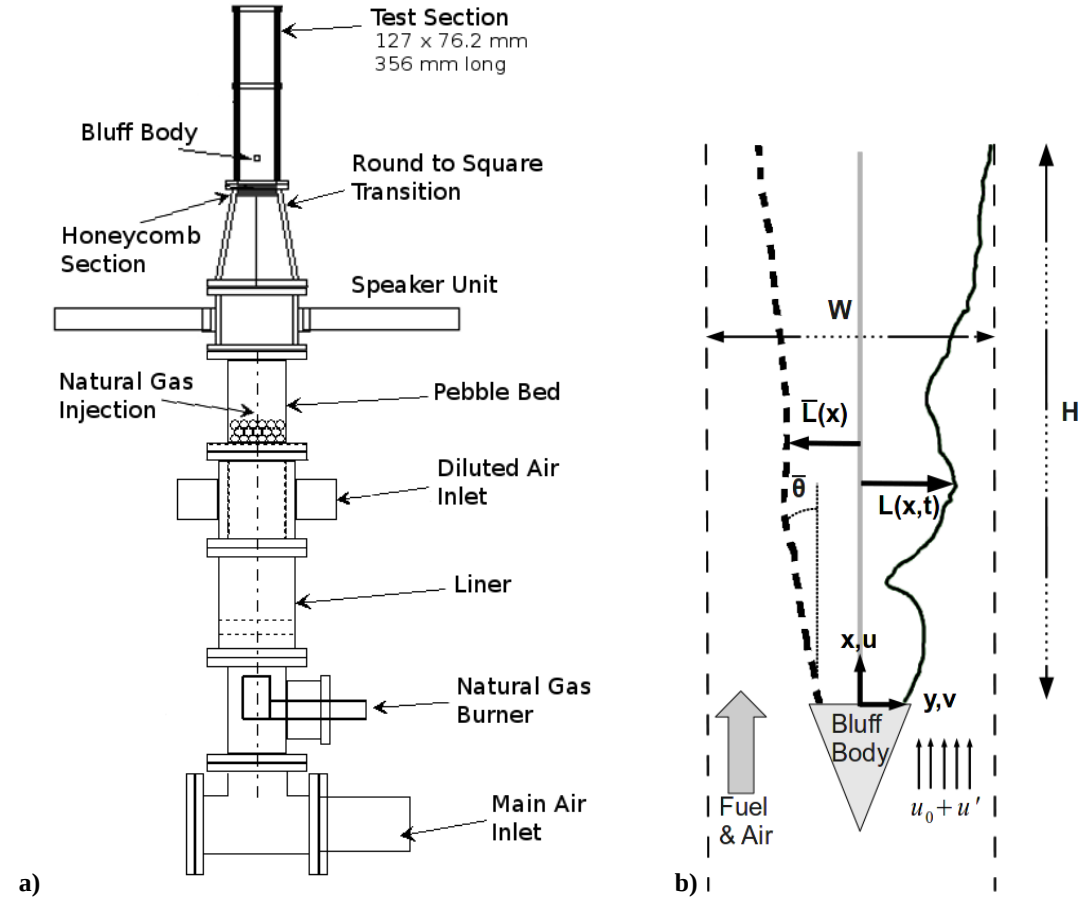

Figure 1. a) Schematic of the ERC experimental facility. b) Schematic of flame and coordinates. The left flame edge (dashed curve) shows an average flame location while the right flame edge (solid curve) shows the instantaneous flame location.

a) Design **b) Installed in test section**

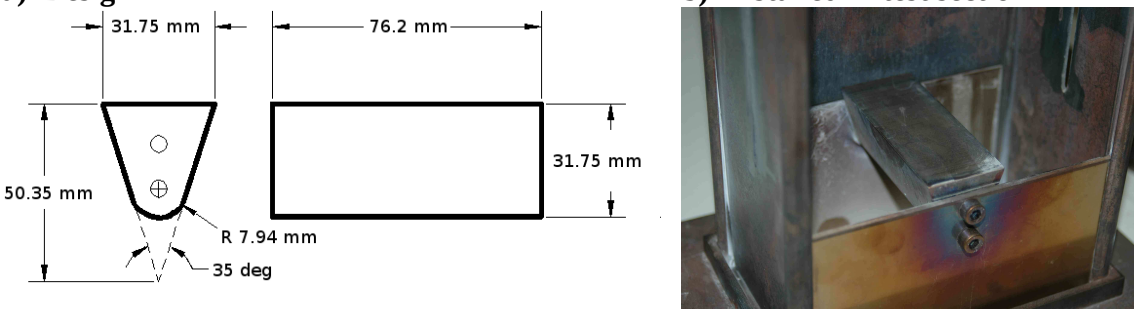

Figure 2. Schematic and photograph of bluff body as installed in the ERC experimental facility.

Longitudinal oscillations are excited with a driver section, installed upstream of the test section. These drivers consist of four 100W Galls Speakers powered by two

Samson Audio Servo 200 Power amplifiers. The signal is generated by a function generator. Acoustic measurements are obtained using a PCB dynamic pressure transducer.

Flame dynamics are determined from direct flame luminosity, recorded with a Vision Research Phantom 7.2 black and white high-speed video camera. The visible (>330 nm) broadband light emission is recorded using a Nikon 35-70mm zoom lens with an f-stop of 3.3. The exposure time is 310 microseconds and the recording rate is 3000 frames per second. A color filter is not used in this study.

Table 1. Summary of flame luminosity experiments, flow conditions and chosen threshold values conducted at the ERC facility. Each experiment set is conducted at two excitation amplitudes (6V and 12V speaker excitation voltage).

Air Flow Rate (kg/s)	Air Flow Velocity at Bluff Body Lip (m/s)	Air Flow Temperature Upstream of Bluff Body (K)	Edge Detection Threshold
0.14	18	294	0.25
0.14	38	644	0.27
0.18	51	644	0.20
0.23	63	644	0.13
0.27	76	644	0.13
0.32	89	644	0.13
0.36	101	644	0.45
0.41	114	644	0.45
0.45	126	644	0.45
0.45	170	866	0.45

Flame Edge Tracking Methodology

The following description closely follows that of previous publications [25-27] and uses the data obtained from the ERC facility. High speed, line-of-sight movies are obtained of acoustically forced flames. Typical images at several flow conditions are shown in Figure 3. In order to determine the dynamics of the flame edge, given by $L(x,t)$, it is necessary to extract the flame edges. This process is complicated by the integration over the line of sight in the image, which causes the edge of the flame in each image to

grow increasingly diffuse with downstream distance due to the growing three-dimensionality of the flame front.

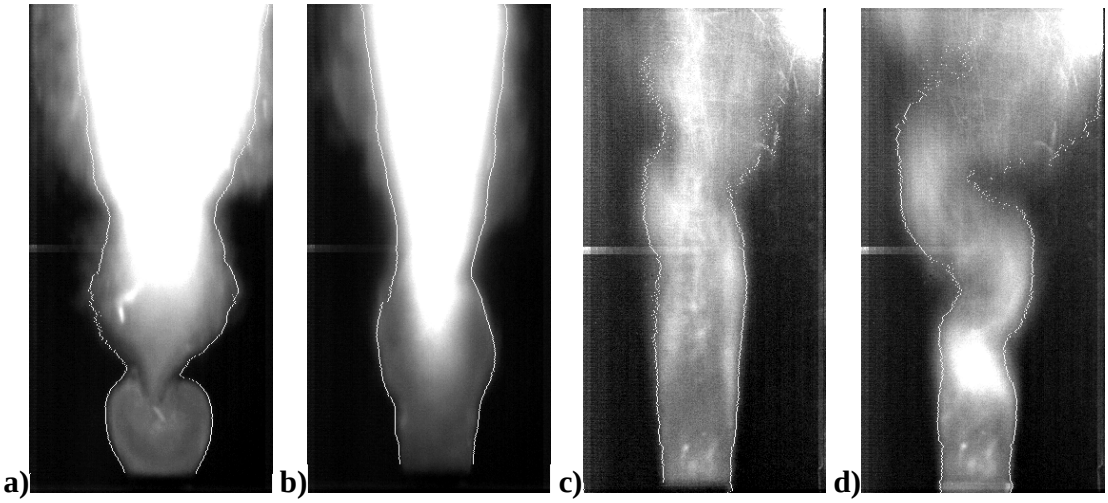

Figure 3. Luminosity flame images and their calculated edges at various flow conditions: a) 18.4 m/s, 294K; b) 38.0 m/s, 644K; c) 127 m/s, 644K; d) 170 m/s, 866K. All cases have a 12V excitation voltage.

These points can be seen in Figure 4, which illustrates a typical flame image and transverse cuts of the smoothed intensity profile at two axial locations. It can be seen that near the bluff body, there is an abrupt discontinuity in image intensity associated with the edge of the flame. Farther downstream, this edge becomes increasingly diffuse. As such, the defined flame edge increasingly becomes a function of the threshold value (see discussion below) with downstream axial distance.

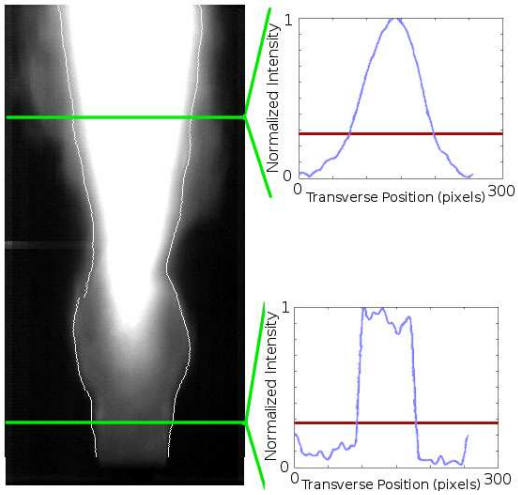

Figure 4. Image intensity at two axial locations. The flame edge location is defined where the intensity (curve) crosses the threshold value (horizontal line), I_t. Flow velocity is 38.0 m/s at 644K and 12V excitation voltage.

We next discuss the specific procedure used for flame edge extraction. First, each row is smoothed with a spatial low-pass filter. Since image intensity changes with downstream distance, the image is normalized to vary between zero and unity at each axial location. Then the flame edge, $L(x,t)$ is defined as the point where the intensity crosses a predefined threshold level, I_t. Note that two flame edges are extracted, associated with the right and left flame branches.

This process is repeated for all rows in a single image and again for all images in a movie and results in a time series for every axial location (x-direction) in an image, as shown in Figure 5a. These time domain data are converted into the frequency domain at each axial location by obtaining the Fourier transform of $L(x,t)$ (see Figure 5b). Note the spike at the forcing frequency, f_0 = 250Hz. The resulting axial dependence of the flame response magnitude (magnitude of the FFT at the forcing frequency) and phase (phase of the FFT at the forcing frequency) are shown in Figure 6.

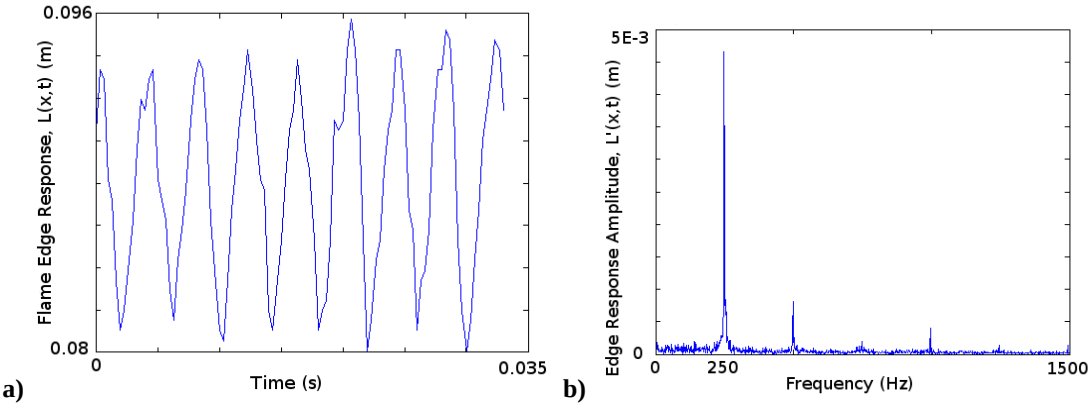

a) **b)**

Figure 5. a) Time series of flame position using I_t = 0.27 at axial location of x/λ_c = 0.47. b) Corresponding spectrum, showing strong response at 250 Hz forcing frequency. Flow conditions: 38 m/s mean flow velocity, 644 K approach temperature, and 12V excitation voltage.

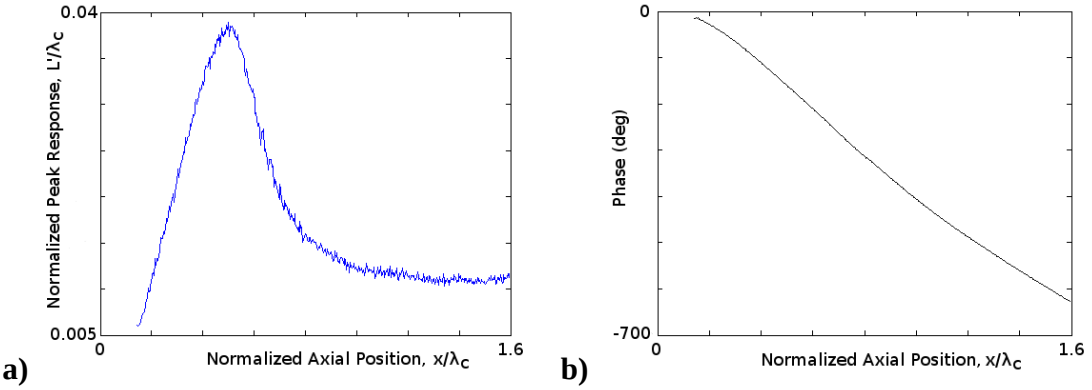

a) **b)**

Figure 6. Normalized flame edge response amplitude (a) and phase (b) at the forcing frequency as a function of normalized downstream distance. Flame edge response amplitude, phase and downstream distance are normalized by the convective wavelength, λ_c. Flow conditions: 38 m/s mean flow velocity, 644 K approach temperature, 12V excitation voltage and I_t = 0.27.

In order to ensure a high quality of results, several techniques are used for checking data validity. First, each point in the time series is checked to make sure it lies further than 10 pixels away from the left or right image border (due to the nature of the data and the edge detection algorithm, many erroneous points default to a value at the image border). If such a point is encountered away from top and bottom image boundaries (i.e., near the center of the image), the gap is filled by interpolating between nearby points. The data is discarded when such events occur in the near-field (starting

with *x=0* and moving along the flame until a first valid point is encountered) of the bluff body and far downstream (starting at the top end of the image and moving down until a first valid point is encountered) where the magnitude of the fluctuations is low. Furthermore, the number of discontinuities and the mode of the time series are computed for each *x*-location. If the number of discontinuities is greater than 1.5% of the total number of points, the result is not reported. Further, the mode of the time series has to be within certain bounds or the result is not reported.

Second, the coherence between the left flame edge and the right flame edge is calculated at the forcing frequency. Only points where the coherence exceeds 0.9 are reported. Typical coherence data is shown in Figure 7. It shows that coherence values are smallest near the bluff body where the magnitude of flame sheet fluctuations is smallest and, therefore, random noise effects are most prominent. It also shows that coherence values generally increase as flow velocities decrease and as the amplitude of excitation increases. In addition, coherence drops far downstream as the flame becomes three-dimensional.

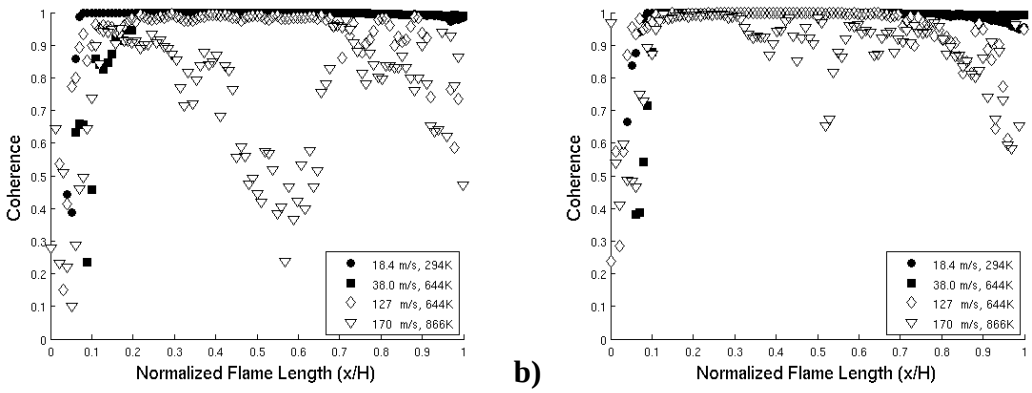

Figure 7. Coherence of the left flame branch to the right flame branch at several flow conditions and a) 6V and b) 12V excitation voltage. Flow conditions: 38 m/s mean flow velocity, 644 K approach temperature.

These results depend upon threshold level, I_t. This sensitivity is illustrated in Figure 8 and Figure 9. Figure 8a shows the axial dependence of the flame response magnitude at the forcing frequency at several threshold values. It shows, as expected, that all results converge in the near-field where the flame is nearly two-dimensional. The curves diverge with downstream distance. Next, it shows that low and high threshold values result in the largest and smallest magnitude of fluctuations, respectively. However, the curves have similar qualitative character, as will be discussed in the next section. Figure 8b shows the corresponding axial phase dependence. This result shows no phase sensitivity to threshold value, except for the highest threshold case.

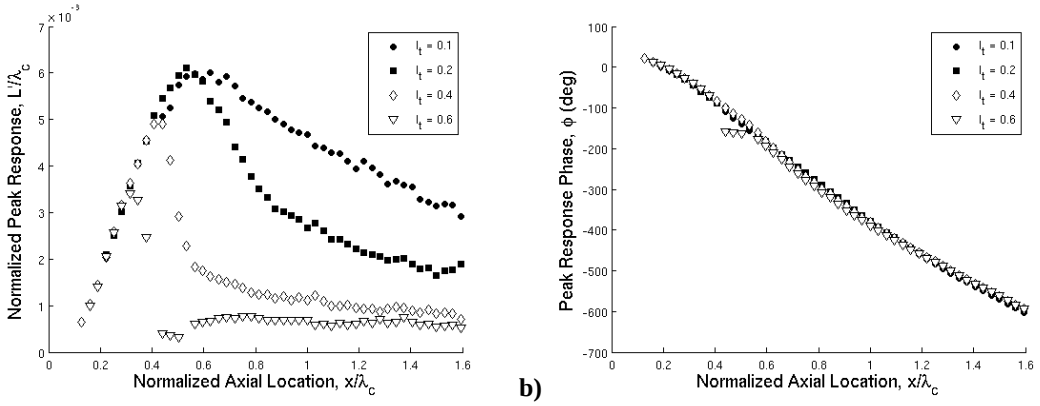

a) **b)**

Figure 8. a) Dependence of flame edge response amplitude on threshold value, I_t. b) Dependence of flame edge response phase on threshold value choice, I_t. Flow conditions: 38 m/s mean flow velocity, 644 K approach temperature, and 12V excitation.

Figure 9 shows the sensitivity of the maximum flame edge response (i.e. maximum of L'/λ_c in Figure 6a) to the threshold value, I_t. For some flow conditions, I_t has little impact on the maximum flame edge response, while for others it is very sensitive to the threshold value choice. Results presented in the next chapter use different threshold values for different flow conditions, reported in Table 1.

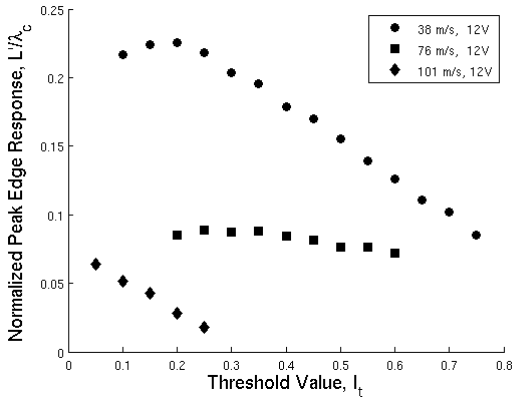

Figure 9. Variation of the peak flame edge response amplitude as a function of threshold value at three different flow conditions.

Flame Luminosity Characterization

In order to alleviate some of the problems stated above, especially related to the arbitrary nature of the thresholding technique and the effect of varying the threshold value, an additional analysis technique is used. Instead of tracking a flame edge, the direct luminosity measurement is used. Overall flame luminosity for these data appears to be related to product gas temperature (not heat release) and volume of gas. Summing the pixel intensities at each axial location produces a flame luminosity function, *Q(x,t)* in space and time. This luminosity is presumably closely correlated with flame position for cases where the left and right flame edges move symmetrically about the centerline. For example, a perturbation in the left flame edge will cause an increase in length of products between the two flame edges at a given height, and therefore luminous product volume.

After this flame luminosity function is obtained, the procedure is similar to the flame edge procedures above. At every axial location, the instantaneous flame luminosity is obtained by summing the pixel values for that row. Figure 10a shows this flame

luminosity as a function of downstream distance. Note the near monotonic increase in luminosity as the flame grows. If this process is repeated, the instantaneous flame luminosity function is obtained as a function of both space and time, $Q(x,t)$. Figure 10b shows Q as a function of time at one downstream location (this is the same location and time instance as shown in Figure 5a).

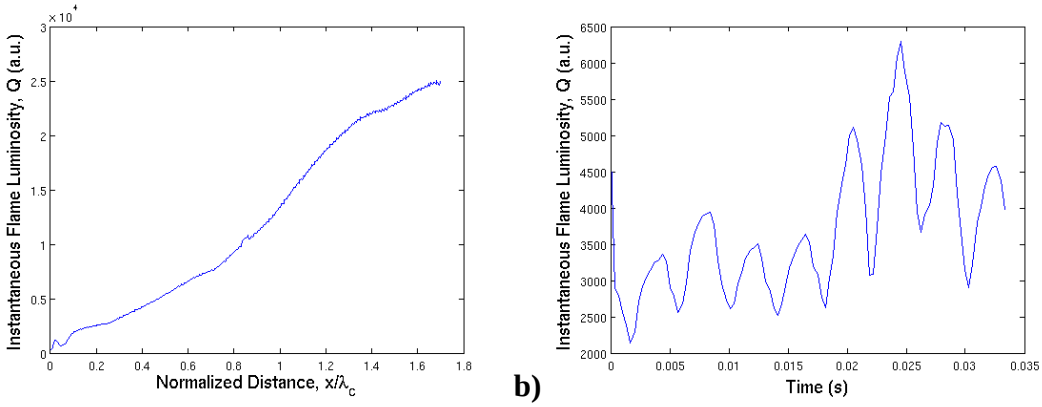

a) **b)**

Figure 10. a) Instantaneous flame luminosity distribution as a function of downstream distance. b) Instantaneous flame luminosity distribution as a function of time at x/λ_c = 0.47. The approach velocity, temperature, and excitation amplitude are 38 m/s, 644K, and 12V, respectively.

Once a time series is obtained, the next step is to use the Fourier transform to calculate the spectrum (Figure 11a). Again, we compare the flame edge spectrum (shown in Figure 5b) directly to the flame luminosity spectrum since they are obtained from the same data set. Both spectra show a very strong peak at the forcing frequency, f_0 and at several harmonic frequencies. One important difference is the increased low frequency noise seen in the flame luminosity spectrum but absent from the flame edge spectrum.

One major difference between the flame edge technique and the flame luminosity technique is in the error elimination step. The flame edge technique details a complicated and multistep data validation algorithm due to the difficulties in obtaining and accurate flame edge. The flame luminosity technique allows for a simpler data validation

algorithm. At every axial location, the signal to noise ratio (defined as the amplitude at the forcing frequency divided by the average noise near the forcing frequency obtained from the spectrum, Figure 11a) is calculated and the results are shown in Figure 11b. When the signal to noise ratio is below 5 (e.g., near $x/\lambda_c = 0.1$) the data is considered to be unreliable and the results at that axial location are not considered. In addition, the first 10-20 pixels in an image are not considered because there is no flame present at that location. These two steps cause discontinuities in the results plots (see Figure 13a and b).

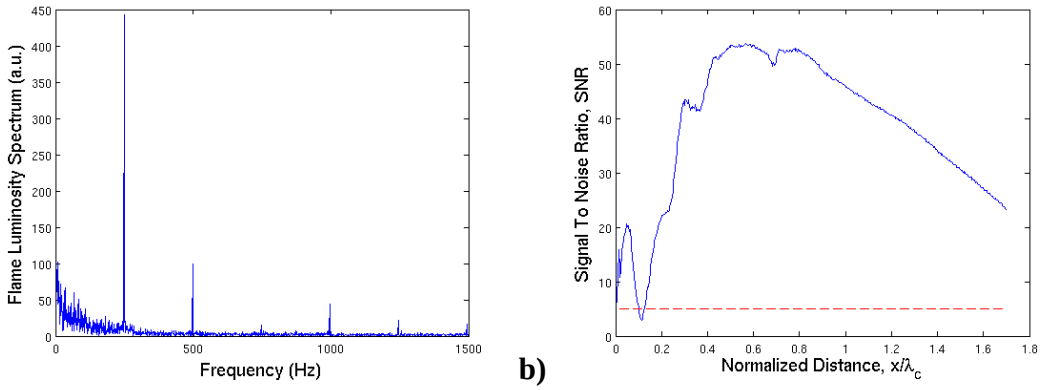

a) **b)**

Figure 11. a) The time series in Figure 10b is converted to the frequency domain at x/λ_c = 0.47. Note the similarities between the flame edge spectrum (Figure 5b) and the flame luminosity spectrum (Figure 11a). b) The signal to noise ratio at the forcing frequency is computed and shown as a function of downstream distance. The minimum SNR is shown as a dashed line. The approach velocity, temperature, and excitation amplitude are 38 m/s, 644K, and 12V, respectively.

Figure 12a shows the flame luminosity fluctuation amplitude derived from the spectrum in Figure 11a. The fluctuation amplitude starts near zero, rises, peaks, and remains nearly constant for the remainder of the viewing window. Figure 12b shows the time averaged flame luminosity as it varies spatially. Note the small spike in average flame luminosity near x/λ_c = 0.8 due to a camera irregularity near the middle of the viewing window (this irregularity is seen in Figure 3 as well).

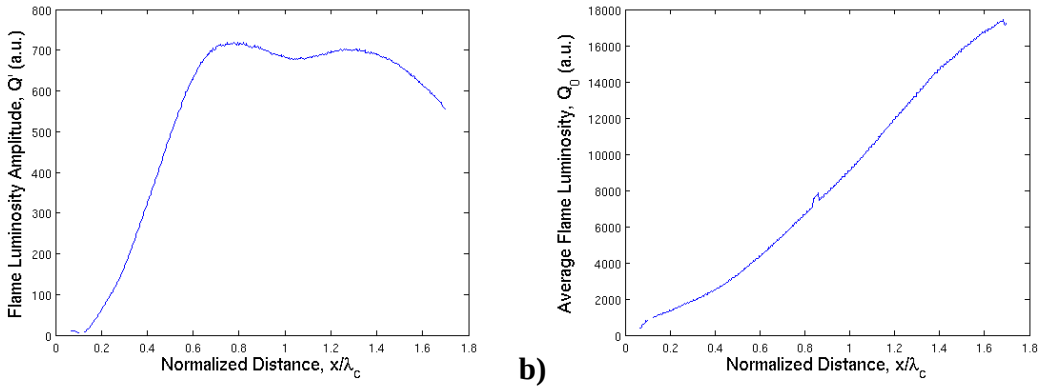

a) **b)**

Figure 12. a) Flame luminosity fluctuation amplitude at the forcing frequency f_0 as obtained from the spectrum in Figure 11a and b) mean flame luminosity as a function of downstream distance. The approach velocity, temperature, and excitation amplitude are 38 m/s, 644K, and 12V, respectively.

Since the directly measured luminosity values are arbitrary, it is necessary to normalize these curves in some manner. To obtain a normalized flame luminosity plot, a localized normalization scheme is used and the ratio of Figure 12a to Figure 12b is taken and the results are shown in Figure 13a. Again, note the small camera irregularity near x/λ_c = 0.8 shown by a dip in the normalized flame luminosity amplitude. While taking the magnitude of the Fourier transform results in the amplitude plot, taking the phase of the transform produces the phase plot in Figure 13b. The phase of the disturbance is related to its convective speed, defined as

$$\frac{u_c}{u_0} = \frac{-360}{(\partial\phi)/(\partial x/\lambda_c)} \tag{4}$$

where $(\partial\phi)/(\partial x/\lambda_c)$ is the slope of the curve in Figure 13b and 360 is a conversion factor.

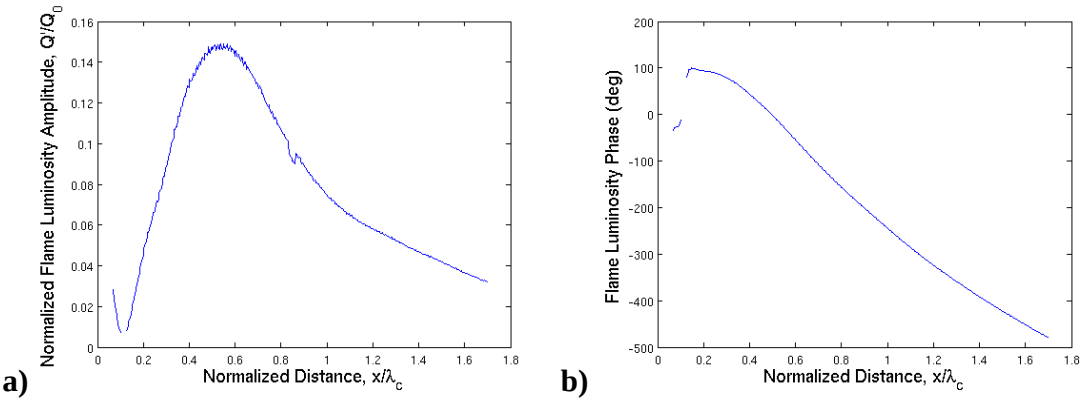

a) **b)**

Figure 13. Normalized flame luminosity amplitude (a) and phase (b) at the forcing frequency as a function of normalized downstream distance. Flame luminosity response amplitude and downstream distance are normalized by the convective wavelength, λ_c. Flow conditions: 38 m/s mean flow velocity, 644 K approach temperature, 12V excitation voltage.

CHAPTER 3

RESULTS

Flame Edge Fluctuations

This section is focused on analyzing the flame transfer function of flame edge fluctuations at several flow velocities and temperature ratios. Figure 14 shows the flame brush from 5 cases under consideration. Several observations can be made from this diagram. First, the location of maximum edge fluctuations varies drastically with the different flow conditions presented. In general, the point of maximum fluctuations moves further downstream with increasing flow velocity. Second, the amplitude of these fluctuations also changes with the different flow conditions. For example, condition c) shows almost no fluctuations, while conditions a) and e) show large fluctuations. Third, at every condition, the base of the flame has zero amplitude, i.e.

$$L'(x=0,t)=0 \tag{5}$$

This observation has important theoretical implications as it allows to make a major simplification of the G equation and a linear solution in the near-field. See [27] for a full discussion on this topic.

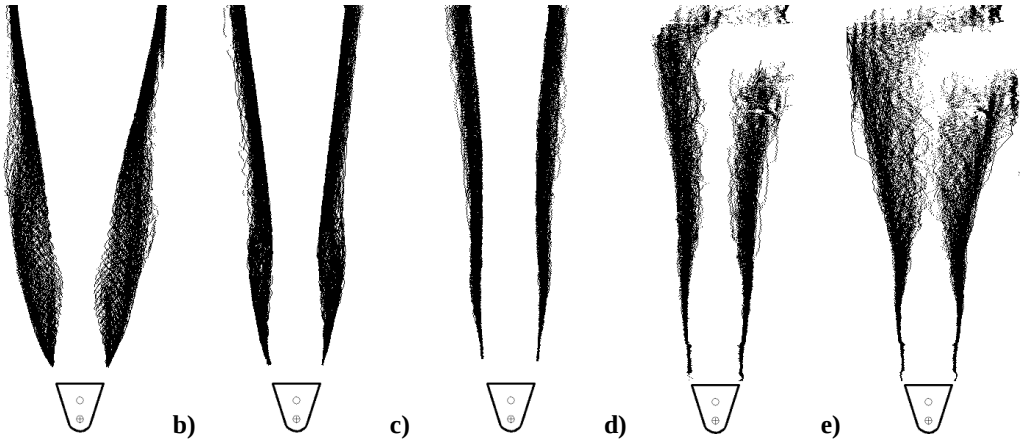

Figure 14. Flame brush of 100 consecutive frames that demonstrate *L'* ~ 0 at *x* = 0 (bluff body trailing edge) for the following conditions: a) 18 m/s, 294K; b) 38 m/s, 644K; c) 76 m/s, 644K; d) 126 m/s, 644K; e) 170 m/s, 866K and 12V speaker excitation voltage. Note that bluff body placement in the above images is approximate.

The "Flame Edge Tracking Methodology" section in Chapter 2 outlines the steps to generate Figure 15 and Figure 16. Flame edge fluctuation amplitude is shown in Figure 15 for several flow velocities and two excitation amplitudes. Several observations can be made from this plot. First, as flow velocity increases, convective wavelength λ_c also increases which shortens the higher velocity plots in the figure, i.e. a smaller convective distance is visible in a constant length test section. Second, all amplitude curves follow the same behavior: from zero amplitude at $x = 0$ there is a linear rise, a peak, and a decay region. The linear rise has been shown to be predictable by a linearized G equation solution by Plaks et.al. [27].

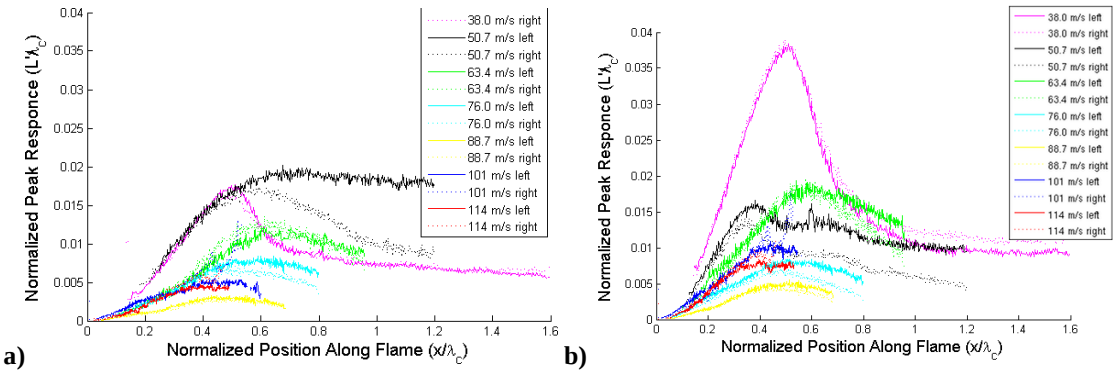

Figure 15. Effect of flow velocity on flame edge response amplitude at a) 6V and b) 12V excitation voltage and inlet temperature of 644 K. The x-coordinate is the downstream distance with x/λ_c = 0 located at the bluff body trailing edge. The left flame edge is represented by a solid line and the right flame edge is represented by a dashed line.

Figure 16 shows the phase of flame edge fluctuations at the forcing frequency f_0. Again, several observations can be made about the resulting data. First, the phase roll-off is nearly constant for the entire length of the flame. This implies that the normalized convective velocity u_c / u_0 is also constant for the entire length of the flame. Second, the normalized convective velocity does not change with mean velocity, i.e. as flow velocity u_0 increases, u_c / u_0 remains constant. Fitting a straight line to the phase results in a convective velocity of $u_c / u_0 = 0.66$.

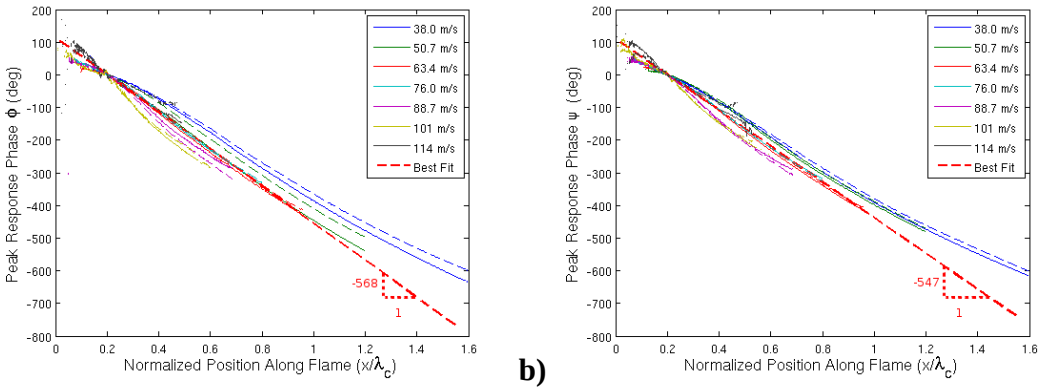

Figure 16. Effect of flow velocity on phase at a) 6V and b) 12V excitation voltage and inlet temperature of 644 K. The *x*-coordinate is the downstream distance with x/λ_c = 0 located at the bluff body trailing edge. The left flame edge is represented by a solid line and the right flame edge is represented by a dashed line. The best fit line is a red dashed line with the slope as indicated. The phase plots are matched for comparison at x/λ_c = 0.2. The slope of the best fit line corresponds to a convective velocity of $u_c / u_0 = 0.66$.

Flame Luminosity Fluctuations

To alleviate the arbitrary nature of flame edge tracking and thresholding the direct flame luminosity is used to obtain a spatial distribution of product gas temperature, which is another measurement of interest.

Similar to Figure 15, Figure 17 shows the flame luminosity fluctuations at the forcing frequency using the methodology described in the previous chapter. Flame luminosity amplitude response shares similarities with flame edge amplitude response: there is an initial rise region, a peak somewhere between $0.2 < x/\lambda_c < 0.7$, and a subsequent decay region. However, not all flame luminosity amplitude curves are zero at $x/\lambda_c = 0$. This is due to a very low average flame luminosity at that location.

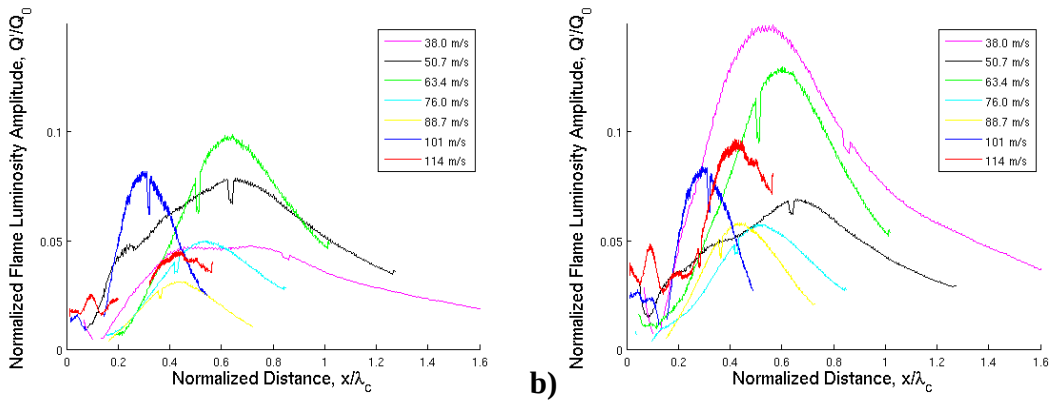

Figure 17. Effect of flow velocity on flame luminosity fluctuations at a) 6V and b) 12V excitation voltage and inlet temperature of 644 K. The x-coordinate is the downstream distance with $x/\lambda_c = 0$ located at the bluff body trailing edge. This plot is comparable to Figure 15 showing flame edge fluctuations.

Figure 18 shows the phases of the respective flame luminosity fluctuations at 6V and 12V excitation voltage. As with flame edge fluctuations, these results are very similar in slopes beyond some initial region. However, there are drastic differences in the initial region where the phase slope is, at times, positive, suggesting that a disturbance is traveling upstream instead of convecting downstream at a convective velocity scaling with the mean flow velocity.

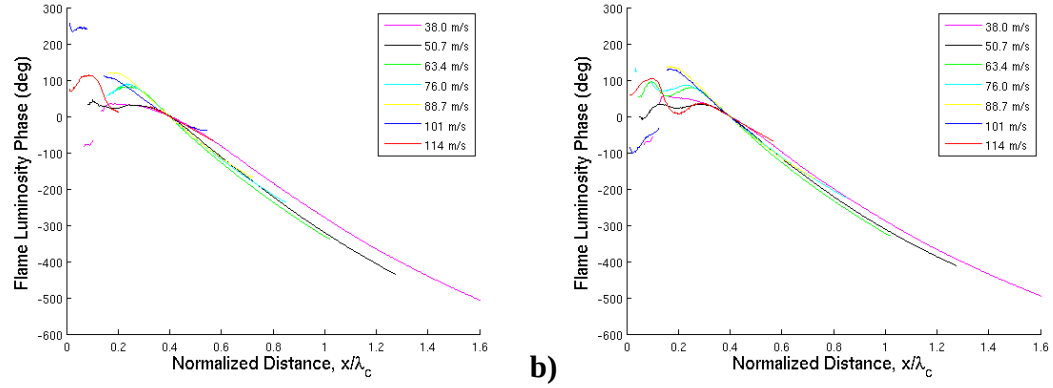

Figure 18. Effect of flow velocity on flame luminosity phase at a) 6V and b) 12V excitation voltage and inlet temperature of 644 K. The *x*-coordinate is the downstream distance with $x/\lambda_c = 0$ located at the bluff body trailing edge. The phase plots are matched for comparison at $x/\lambda_c = 0.4$. This plot is comparable to Figure 16 showing flame edge fluctuations.

In previous studies dealing with this data [26, 27] no accurate results were obtained at flow velocities above 114 m/s due to poorly defined flame edges and poor flame edge tracking. However, measuring flame luminosity does not require an accurate flame edge and the obtained results are shown in Figure 19. These results follow those at lower flow velocities. Flame luminosity amplitude starts at a non-zero value (again, due to a very low average flame luminosity near x/λ_c = 0), grows, peaks, and decays. Similarly, the phase has a very non-linear region in the near-field and has a linear decay in the far-field region.

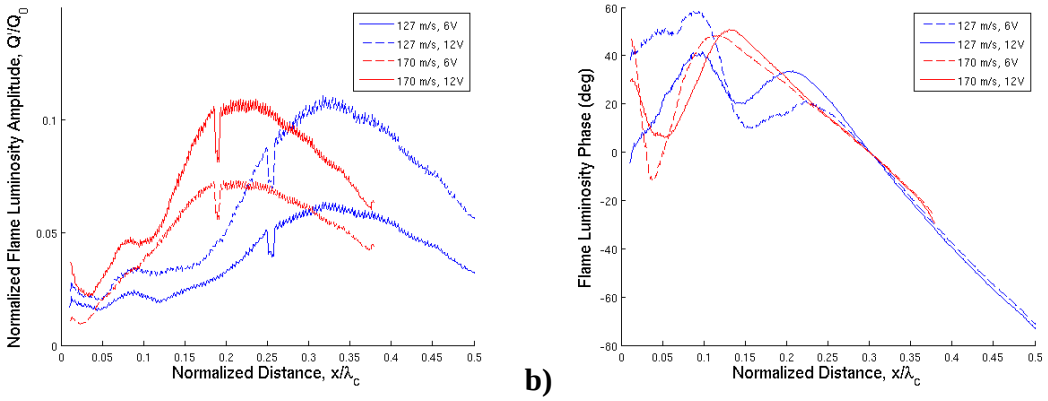

a) **b)**

Figure 19. Flame luminosity fluctuation amplitude a) and phase b) as a function of downstream distance at two flow conditions, 127 m/s at 644 K and 170 m/s at 866 K and two excitation voltages: 6V and 12V. The phase plots are matched for comparison at x/λ_c = 0.3.

Comparison of Flame Luminosity and Flame Edge Fluctuations

Since scaling between flame edge fluctuations and flame luminosity fluctuations is not yet determined, to properly compare them, each amplitude curve is normalized by its maximum such that it has values between zero and unity.

Figure 20 shows a typical low velocity comparison between flame edge fluctuations and flame luminosity fluctuations. No accurate flame edge data is available

for x/λ_c < 0.2 at this flow condition. Between 0.2 < x/λ_c < 0.5, the two fluctuation magnitudes agree perfectly: the slope in the initial linear region and the peak amplitude location coincide. However, x/λ_c > 0.5, the two curves diverge. This is somewhat expected as the decay region in the flame edge response curve is highly dependent on the threshold value, I_t. In fact, by carefully choosing a proper threshold value the flame edge amplitude curve and the flame luminosity amplitude curve will coincide.

Figure 21 rescales the curves in Figure 8a by their respective maxima such that each curve is between zero and unity. As previously concluded, at 38 m/s, increasing the threshold value I_t has two effects: the peak amplitude is decreased and the decay region becomes steeper while the initial rise region remains unchanged. Since Figure 21 rescales these amplitude curves by their respective maxima, the initial slope is changed. This effect is acceptable since the intended goal is to compare qualitative features between flame edge fluctuations and flame luminosity fluctuations. In this rescaled plot (Figure 21) as I_t is increased, the initial slope increases while the peak location moves upstream and the decay region becomes steeper. However, there is a threshold choice that makes the flame edge amplitude plot and the flame luminosity amplitude plot coincide.

Additionally, Figure 20b shows the phases of flame fluctuations and flame luminosity fluctuations. In the near-field, x/λ_c < 0.3, there is little to no agreement between the slopes of the two sets of curves. Beyond this point, however, there is great agreement between the two curves.

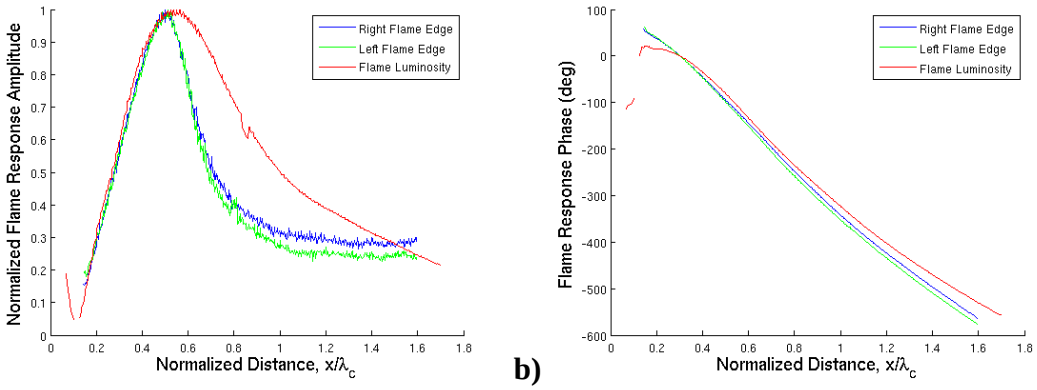

a) **b)**

Figure 20. Comparison of flame luminosity fluctuations to flame edge fluctuations. a) Amplitude response is normalized by its respective peak. b) Phases are matched at x/λ_c = 0.3. Flow conditions: 38 m/s mean flow velocity, 644 K approach temperature, 12V excitation voltage.

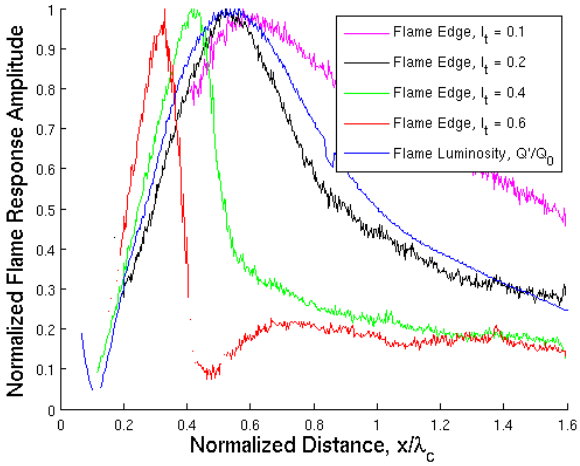

Figure 21. Variation of the flame edge response curve due to varying the flame edge threshold value, I_t. This figure is derived from Figure 8a. Each curve is normalized by its maximum such that it is scaled from zero to unity. Flow conditions: 38 m/s mean flow velocity, 644 K approach temperature, 12V excitation voltage.

At most low velocity flow conditions (u_0 < 100 m/s), there is good agreement between flame edge fluctuations and flame luminosity fluctuations as further demonstrated in Figure 22a. There is good agreement between the phases of flame edge fluctuations and flame luminosity fluctuations beyond some initial region (see Figure 22b).

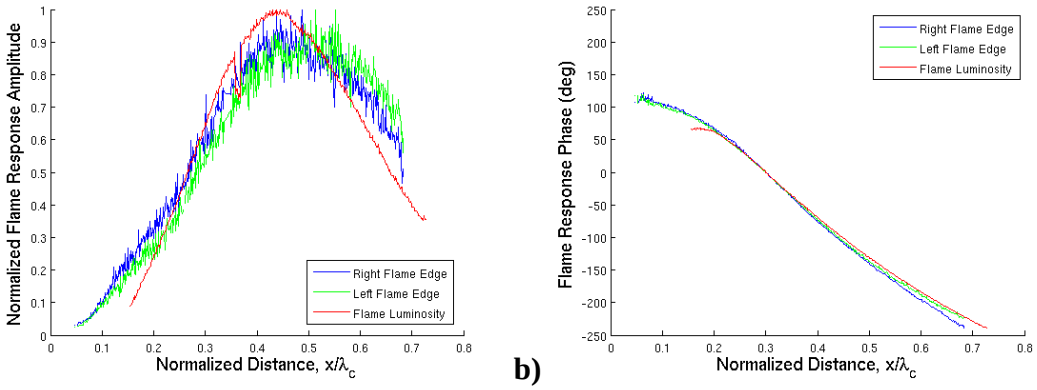

a) **b)**

Figure 22. Comparison of flame luminosity fluctuations to flame edge fluctuations. a) Amplitude response is normalized by its respective peak. b) Phases are matched at x/λ_c = 0.3. Flow conditions: 89 m/s mean flow velocity, 644 K approach temperature, 12V excitation voltage.

At high flow velocities (u_0 > 100 m/s), there is little agreement in amplitude plots between flame edge fluctuations and flame luminosity fluctuations as seen in Figure 23a. However, Figure 23b still shows good agreement between the two phase curves beyond some initial region. However, unlike low velocity cases, Figure 24 demonstrates that the threshold cannot be varied enough to get flame edge fluctuations to coincide with flame luminosity fluctuations. Similar to low velocity results, the phases (Figure 23b) are very similar beyond x/λ_c > 0.15.

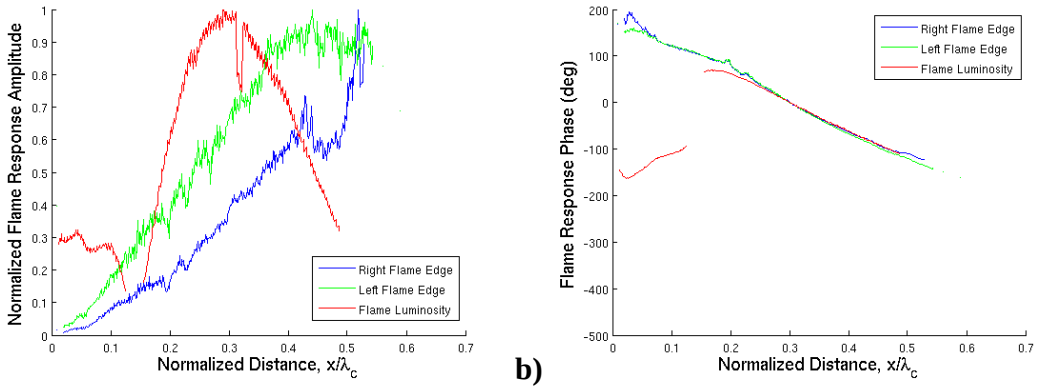

a) **b)**

Figure 23. Comparison of flame luminosity fluctuations to flame edge fluctuations. a) Amplitude response is normalized by its respective peak. b) Phases are matched at x/λ_c = 0.3. Flow conditions: 101 m/s mean flow velocity, 644 K approach temperature, 12V excitation voltage.

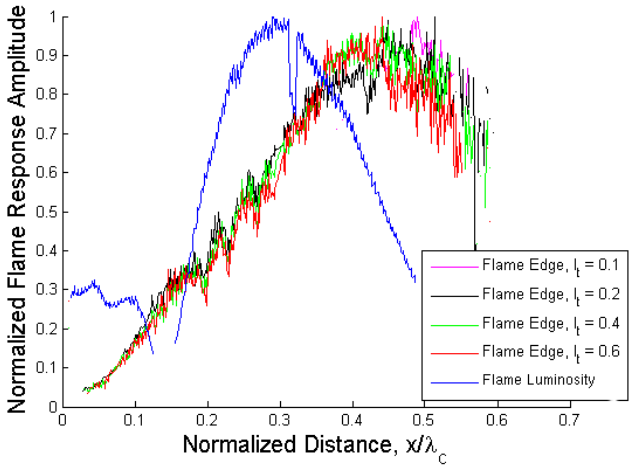

Figure 24. Variation of the flame edge response curve due to varying the flame edge threshold value, I_t. This figure is similar to Figure 21. Each curve is normalized by its maximum such that it is scaled from zero to unity. Flow conditions: 101 m/s mean flow velocity, 644 K approach temperature, 12V excitation voltage.

Comparison to Model Data

The basic approach to modeling the flame response is to use the G equation. This approach has been used many times in previous studies [28-31] and further discussion in this section closely follows the work of Shin [11, 26, 27, 32].

The relationship between heat release fluctuations and flame area is:

$$Q' = \oint h_R \rho S_L \, dA \tag{6}$$

where h_R is the heat of reaction, ρ is the fluid density, S_L is the laminar flame speed and dA is an infinitesimal flame area. This infinitesimal flame area, when integrated over the entire flame, shows flame area fluctuations. For a two-dimensional flame, flame edge fluctuations and flame area fluctuations are equal. While assuming that heat of reaction and density are constant is valid, the afterburner flame is highly turbulent and using a laminar flame speed is erroneous. In order to use equation (6) to relate heat release and

flame edge fluctuations, a turbulent flame speed model is typically used; however, this model is highly complicated and beyond the scope of this thesis.

For a two dimensional flame, the instantaneous flame position *L*, is given by a first order partial differential equation

$$\frac{\partial L}{\partial t} + u\frac{\partial L}{\partial x} - v = S_L\sqrt{\left(\frac{\partial L}{\partial x}\right)^2 + 1} \tag{7}$$

The coordinate system is shown in Figure 1b. In the near-field, the G equation is linearized and characterizes the flame dynamics in this region. The slope of the $\left|L'(x, f_0)\right|$ vs. *x* curve in the near-field is derived as

$$\frac{\partial\left|L'(x=0, f)\right|}{\partial x} = \frac{\left|u_n'(x=0, f)\right|}{u_{t,0}(x=0)}\frac{1}{\cos^2\theta} \tag{8}$$

This equation assumes that $L'(x=0, f)=0$ (i.e. at the flame attachment point there are no flame fluctuations), which is experimentally verified in Figure 14. The location of peak response amplitude can be predicted via

$$x_{peak}/\lambda_c = \frac{\cos^2\theta}{2\left|\frac{u_0}{u_{c,v}}\cos^2\theta - 1\right|} \tag{9}$$

However, in order to capture non-linear effects in the far-field, it is necessary to solve the full G equation numerically. While the full details of the numerical scheme and full model details are outlined by Shin [27], they are presented here as a convenience. Figure 25 shows great agreement between experimentally measured flame edge fluctuations and numerically obtained predictions in the near-field. The location of maximum flame edge fluctuations is also predicted well. However, an "undamped" model (represented by ■) predicts a second amplitude peak in the far-field that is not

supported by experimental results. This undamped model assumes a constant perturbation velocity, v'/u_0 for the entire length of the flame.

Better agreement between theory and experimental data is achieved with a "damped" velocity perturbation model (represented by ◆) where v'/u_0 is constant for $x/\lambda_c < 0.82$ and zero for $x/\lambda_c > 0.82$. However, this velocity field does not appear to be consistent with measured velocity profiles (see Figure 25b), indicating that far-field flame response predictions is an item requiring future work.

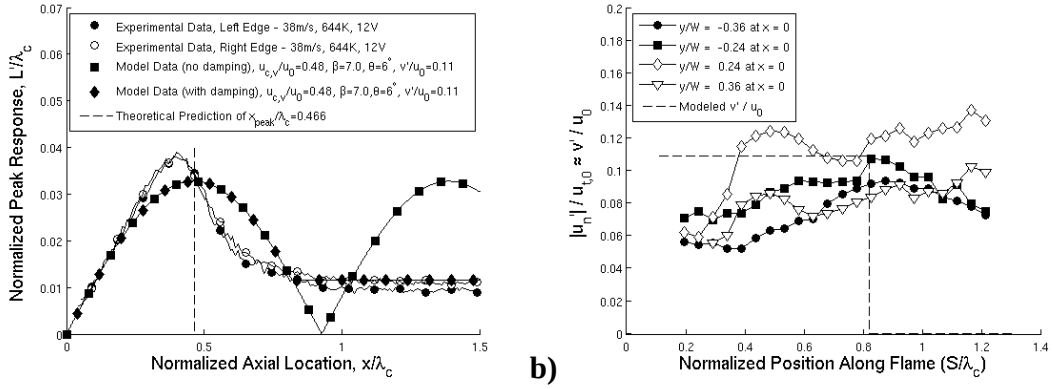

a) **b)**

Figure 25. a) Comparison of experimentally measured and theoretically calculated flame edge response at u_0 = 38 m/s and 12V excitation voltage. x_{peak} location is predicted by Eq. (9). b) Modeled velocity fluctuations used to obtain results in a) compared to experimentally obtained velocity fluctuations.

The above model requires the knowledge of the velocity field near the flame. This information was obtained from a previous study [27]; however, it is only available at one flow condition and thus it is not possible to compare model predictions at different flow velocities.

CHAPTER 4

CONCLUSIONS

This thesis characterizes the transfer function of a longitudinally forced bluff body stabilized flame. The key contributions of this work are:

1. Measured the flame edge fluctuations and flame luminosity fluctuations of longitudinally forced bluff body flames under realistic afterburner conditions.
2. Compared flame edge fluctuations to current theory and showed where further improvements in theory are necessary.

Two methods are used to quantify flame fluctuations at the forcing frequency. Flame edge fluctuations allow a direct comparison between experimental data and numerically calculated model results. The flame edge amplitude has a quantitatively similar behavior between different flow conditions: flame edge amplitude is zero at the trailing edge of the bluff body, it rises monotonically, peaks, and decays. The flame edge phase is nearly linear for the entire length of the flame and results in a constant flame wrinkle convective velocity on the order of the mean flow velocity. However, since the definition of the flame edge is somewhat arbitrary, the results depend upon the utilized threshold value. The flame edge amplitude has the greatest sensitivity to the threshold choice as it affects the peak response amplitude and the decay region. The threshold choice has little effect on the near-field region.

To eliminate some of the problems with the flame edge methodology, the flame luminosity distribution is utilized. It is a direct measurement of interest, improves

accuracy, and reduces computational time. There is great agreement between flame edge amplitude and flame luminosity amplitude response at flow velocities below 100 m/s. However, above 100 m/s, the accuracy of the flame edge method is greatly diminished and the flame luminosity results greatly differ from the flame edge results. The phase of flame luminosity fluctuations differs from flame edge fluctuations in the near-field, at times suggesting a negative convective velocity, however, the two agree well in the far-field. Due to the increased accuracy of the flame luminosity method, two more flow conditions (127 m/s and 170 m/s) that were left out of previous studies are characterized. Their results are qualitatively similar to lower flow velocity conditions.

Finally, the experimental results are compared to model data. Since the numerical model requires knowledge of the velocity field, a quantitative comparison between the two are only possible at one flow condition. Flame edge amplitude matches closely to the theoretically predicted amplitude in the near-field. The peaks of the two amplitudes also match but the results differ greatly in the far-field.

Future work in this area should focus on further exploring the difference between flame edge fluctuations and heat release fluctuations (using a CH* camera filter will provide heat release data). In addition, characterizing the transfer function of a transversely forced flame as it is more applicable to real world conditions. The same analysis detailed in this study can be readily applied to a transversely forced flame and should lead to a greater understanding of afterburner flames. Further, measuring the velocity field via PIV at more flow conditions will allow for better comparison between theory and experiments and should lead to a more refined model.

REFERENCES

[1] V. N. Kornilov, M. Manohar and L. P. H. de Goey. Thermo-acoustic behaviour of multiple flame burner decks: Transfer Function (de)composition. *Proceedings of the Combustion Institute*, 2009, 32(1), 1383-1390.

[2] C. M. Coats, Z. Chang and P. D. Williams. Excitation of thermoacoustic oscillations by premixing domestic gas burners. *Combustion Science and Technology*, 2008, 180(2), 314-342.

[3] V. N. Kornilov, K. R. A. M. Schreel and L. P. H. De Goey. Experimental assessment of the acoustic response of laminar premixed Bunsen flames. Heidelberg, Germany, 2007.

[4] C. A. Armitage, R. Balachandran, E. Mastorakos and R. S. Cant. Investigation of the nonlinear response of turbulent premixed flames to imposed inlet velocity oscillations. *Combustion And Flame*, 2006, 146(3), 419-436.

[5] R. Balachandran, B. O. Ayoola, C. F. Kaminski, A. P. Dowling and E. Mastorakos. Experimental investigation of the nonlinear response of turbulent premixed flames to imposed inlet velocity oscillations. *Combustion And Flame*, 2005, 143(1-2), 37-55.

[6] R. Balachandran, A. P. Dowling and E. Mastorakos. Non-linear response of turbulent premixed flames to imposed inlet velocity oscillations of two frequencies. *Flow Turbulence and Combustion*, 2008, 80(4), 455-487.

[7] B. B. Dally, A. R. Masri, R. S. Barlow and G. J. Fiechtner. Instantaneous and mean compositional structure of bluff-body stabilized nonpremixed flames. *Combustion And Flame*, 1998, 114(1-2), 119-148.

[8] H. Y. Wang, C. K. Law and T. Lieuwen. Linear response of stretch-affected premixed flames to flow oscillations. *Combustion And Flame*, 2009, 156(4), 889-895.

[9] A. Birbaud, D. Durox, S. Ducruix and S. Candel. Dynamics of confined premixed flames submitted to upstream acoustic modulations. *Proceedings of the Combustion Institute*, 2007, 31(1), 1257-1265.

[10] S. J. Shanbhogue and T. Lieuwen. Response of a Rod Stabilized, Premixed Flame to Longitudinal Acoustic Forcing. *ASME Turbo Expo: Power for Land, Sea and Air*, Barcelona, Spain, 2006.

[11] S. J. Shanbhogue, D.-H. Shin, S. Hemchandra, D. Plaks and T. Lieuwen. Flame-sheet dynamics of bluff-body stabilized flames using longitudinal acoustic forcing. *Proceedings of the Combustion Institute*, 2009.

[12] V. Shteinberg and P. Kim. Regions of self-excitation of a singing flame. *Heat Transfer Research*, 2008, 39(7), 627-637.

[13] S. R. Chakravarthy, R. Sivakumar and O. J. Shreenivasan. Vortex-acoustic lock-on in bluff-body and backward-facing step combustors. *Sadhana-Academy Proceedings in Engineering Sciences*, 2007, 32(1-2), 145-154.

[14] W. Pun, S. Palm and F. Culick. Combustion dynamics of an acoustically forced flame. *Combust. Science & Tech.*, 2003, 175(3), 499-521.

[15] Preetham. Modeling the response of premixed flames to flow disturbances. Georgia Institute of Technology. Atlanta, Ga. 2007.
[16] S. J. Shanbhogue, S. Husain and T. Lieuwen. Lean blowoff of bluff body stabilized flames: Scaling and dynamics. *Progress in Energy and Combustion Science*, 2009, 35(1), 98-120.
[17] J. A. Lovett, T. P. Brogen, D. S. Philippona, B. V. Kiel and T. V. Thompson. Development Needs for Afterburner Designs. *40th AIAA/ASME/SAE/ASEE Joint Propulsion Conference and Exhibit*, Ft Lauderdale, FL, 2004.
[18] T. Lieuwen, S. Shanbhogue, S. Khosla and C. Smith. Dynamics of Bluff Body Flames near Blowoff. *45th AIAA Aerospace Sciences Meeting and Exhibit*, Reno, NV, 2007.
[19] A. Prasad and C. Williamson. The instability of the shear layer separating from a bluff body. *Journal of Fluid Mechanics*, 1997, 333, 375-402.
[20] T. Von Karman. Über den Mechanismus des Widerstandes, den ein bewegter Körper in einer Flüssigkeit erfährt. *Nachrichten der Kaiserlichen Gesellschaft der Wissenschaften zu Göttingen S*, 1911, 324–338.
[21] R. R. Erickson, M. C. Soteriou and P. G. Mehta. The Influence of Temperature Ratio on the Dynamics of Bluff Body Stabilized Flames. *44th AIAA Aerospace Sciences Meeting & Exhibit*, Reno, Nevada, 2006.
[22] C. Smith, D. Nickolaus, T. Leach, B. Kiel and K. Garwick. Les Blowout Analysis of Premixed Flow Past V-Gutter Flameholder. 2007.
[23] S. Khosla, T. Leach and C. Smith. Flame Stabilization and Role of von Karman Vortex Shedding Behind Bluff Body Flame Holders. *43rd AIAA/ASME/SAE/ASEE Joint Propulsion Conference & Exhibit*, Cincinnati, OH, 2007.
[24] J. M. Beér and N. A. Chigier. *Combustion aerodynamics*. Halsted Press Division, New York,, 1972.
[25] C. T. Brown, V. G. McDonell and B. Kiel. Test Bed for Characterization of Liquid Jet Injection Phenomenon at Augmentor Conditions. *42nd AIAA/ASME/SAE/ASEE Joint Propulsion Conference and Exhibit*, Sacramento, California, 2006.
[26] T. Lieuwen, D. Plaks, D. H. Shin, U. M. Mondragon, C. T. Brown, V. G. McDonell and S. Kiel. Dynamics of a Longitudinally Forced, Bluff Body Stabilized Flame. *47th AIAA Aerospace Sciences Meeting*, Orlando, FL, 2009.
[27] D. Plaks, D. H. Shin, T. Lieuwen, U. M. Mondragon, C. T. Brown and V. G. McDonell. Dynamics of a Longitudinally Forced, Bluff Body Stabilized Flame. 2009 (Under Review).
[28] M. Fleifil, A. M. Annaswamy, Z. A. Ghoneim and A. F. Ghoneim. Response of a laminar premixed flame to flow oscillations: A kinematic model and thermoacoustic instability results. *Combustion And Flame*, 1996, 106, 487-510.
[29] S. Ducruix, D. Durox and S. Candel. Theoretical and experimental determination of the transfer function of a laminar premixed flame. *Proceedings of the Combustion Institute*, 2000, 28, 765-773.
[30] V. Yang and F. E. C. Culick. Analysis of low frequency combustion instabilities in a laboratory ramjet combustor. *Combustion Science and Technology*, 1986, 45(1), 1-25.

[31] T. Lieuwen. Physics of Premixed Combustion - Acoustic Wave Interactions. In T. Lieuwen and V. Yang, eds. *Combustion Instabilities in Gas Turbine Engines: Operational Experience, Fundamental Mechanisms, and Modeling* American Institute of Aeronautics and Astronautics, Arlington, TX, 2005.

[32] D. H. Shin, S. J. Shanbhogue and T. Lieuwen. Premixed Flame Kinematics in an Axially Decaying, Harmonically Oscillating Vorticity Field. *44th AIAA/ASME/SAE/ASEE Joint Propulsion Conference & Exhibit*, Hartford, Connecticut, 2008.